

Module-Assembled Elastomer Showing Large Strain Stiffening Capability and High Stretchability

Shintaro Nakagawa,* Daisuke Aoki, Yuki Asano, and Naoko Yoshie

Elastomers are indispensable materials due to their flexible, stretchable, and elastic nature. However, the polymer network structure constituting an elastomer is generally inhomogeneous, limiting the performance of the material. Here, a highly stretchable elastomer with unprecedented strain-stiffening capability is developed based on a highly homogeneous network structure enabled by a module assembly strategy. The elastomer is synthesized by efficient end-linking of a star-shaped aliphatic polyester precursor with a narrow molecular-weight distribution. The resulting product shows high strength (≈ 26 MPa) and remarkable stretchability (stretch ratio at break $\approx 1900\%$), as well as good fatigue resistance and notch insensitivity. Moreover, it shows extraordinary strain-stiffening capability (>2000 -fold increase in the apparent stiffness) that exceeds the performance of any existing soft material. These unique properties are due to strain-induced ordering of the polymer chains in a uniformly stretched network, as revealed by in situ X-ray scattering analyses. The utility of this great strain-stiffening capability is demonstrated by realizing a simple variable stiffness actuator for soft robotics.

polymer chains. Their mechanical properties largely depend on the network structure and the chemical structure of the constituting polymer chains. Conventional elastomers are typically produced by random bonding between linear polymer chains that inevitably leads to a variety of heterogeneities in the network structure (Figure 1a). For example, dangling chains do not contribute to the elasticity, and nonuniformity of the chain length between crosslinks causes stress concentration upon deformation and leads to catastrophic failure. Various strategies have been developed to enhance the performance of elastomers. Addition of rigid micro/nanoparticles such as carbon black was the first breakthrough in the early 20th century, dramatically improving key properties including elastic modulus, tensile strength, and abrasion resistance.^[1] More recently, weak reversible interactions such as hydrogen bonds,^[2,3] coordination

bonds,^[4] and ionic interactions^[5] have been introduced as physical crosslinks in elastomers to realize toughness and novel dynamic functions like self-healing ability. These strategies, however, do not resolve the fundamental problems caused by network heterogeneities.

The past couple of decades have seen great advances in controlling the network structure in crosslinked polymers. The most promising technique to reduce heterogeneity is the module assembly strategy^[6–8] (Figure 1b). When the chain ends of multi-arm polymers with a narrow molecular-weight distribution (“modules”) are conjugated in solution, the resultant network ideally has no dangling chains and the chain length between adjacent crosslinks is uniform. This simple yet powerful strategy has now become a convenient tool to fabricate gel materials with predictable properties.^[8,9] However, application of this module assembly strategy to solvent-free elastomers has rarely been pursued. Because polymer chains are much more densely packed in elastomers than in gels, it is possible to unlock unprecedented mechanical properties using solvent-free elastomers with homogeneous networks.

Herein, we developed a module-assembled elastomer synthesized by end-linking of monodisperse multi-arm polymers. The elastomer showed excellent stretchability, high strength, and unusually large and abrupt strain-stiffening behavior that have yet to be demonstrated by any other existing soft materials. By in situ structural analysis of the elastomer under tension, we found that these properties were caused by strain-induced ordering of


1. Introduction

Since the serendipitous discovery of vulcanization of natural rubber in the 19th century, elastomers have been an indispensable class of material due to their flexible, stretchable, and elastic nature. Elastomers consist of a 3D crosslinked network of flexible

S. Nakagawa, N. Yoshie
Institute of Industrial Science
The University of Tokyo
4-6-1 Komaba, Meguro-ku, Tokyo 153-8505, Japan
E-mail: snaka@iis.u-tokyo.ac.jp

D. Aoki
Graduate School of Engineering
Chiba University
1-33 Yayoi-cho, Inage-ku, Chiba 263-8522, Japan

Y. Asano
Graduate School of Engineering
The University of Tokyo
7-3-1 Hongo, Bunkyo-ku, Tokyo 113-8656, Japan

 The ORCID identification number(s) for the author(s) of this article can be found under <https://doi.org/10.1002/adma.202301124>

© 2023 The Authors. Advanced Materials published by Wiley-VCH GmbH. This is an open access article under the terms of the Creative Commons Attribution-NonCommercial License, which permits use, distribution and reproduction in any medium, provided the original work is properly cited and is not used for commercial purposes.

DOI: 10.1002/adma.202301124

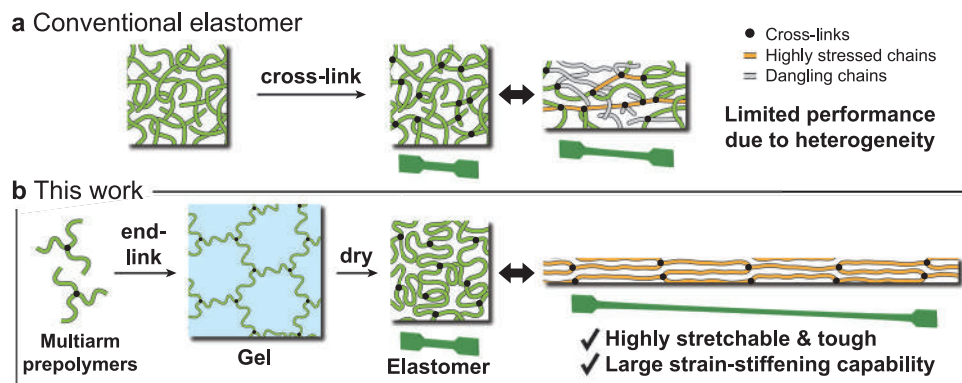


Figure 1. Concept of this study. a) Conventional elastomer. An amorphous low- T_g polymer is cross-linked randomly, resulting in a highly heterogeneous polymer network. Upon stretching, stress becomes concentrated in a small number of chains, and some chains do not carry the stress. b) Homogeneous elastomer developed in this work. End-linking of noncrystallizable low- T_g multi-arm prepolymers yields a highly homogeneous gel, which is then dried to obtain a solvent-free elastomer. A uniform stress distribution is expected upon stretching.

polymer chains in a uniformly stretched network. We demonstrated the use of this elastomer in a variable stiffness actuator that leveraged its significant strain-stiffening capability.

2. Preparation and Mechanical Performance of the Elastomer

Our elastomers were fabricated by end-linking 3-arm or 4-arm precursor polymers with narrow molecular-weight distributions (Figure 2a). We chose poly(4-methyl- ϵ -caprolactone) (PMCL) as the main polymer component because of its noncrystallizable nature and low glass-transition temperature (T_g), both of which are necessary to fabricate elastomers. In addition, PMCL is an environmentally friendly polymer because it undergoes enzymatic degradation^[10] and its monomer, 4-methyl- ϵ -caprolactone (MCL), can potentially be produced from biomass.^[11] Multi-arm PMCLs were synthesized by acid-catalyzed ring-opening polymerization of MCL from triol or tetraol. The hydroxy groups at each chain end were then modified with a phenylmaleimide (PhMal) moiety.^[12,13] We synthesized three precursor polymers: 3-arm with $M_n = 32$ kDa, 4-arm with $M_n = 24$ kDa, and 4-arm with $M_n = 44$ kDa. We refer to these precursors as 3-arm 30k, 4-arm 20k, and 4-arm 40k, respectively. The synthesis and characterization of these precursor polymers can be found in the Supporting Information (Section S1 and Table S1, Supporting Information).

The precursor was mixed with a low-molar-mass dithiol linker (3,6-dioxa-1,8-octanedithiol, DODT) in dimethylformamide (DMF) solution. A highly efficient thiol-maleimide coupling reaction^[14] led to gelation of the mixture within ≈ 30 min. After curing at r.t. for 1 day, the gel was washed and dried to obtain a solvent-free elastomer. The gel fraction of the synthesized elastomer was gravimetrically determined to be $\approx 96\%$ for the case of the 3-arm 30k precursor, indicating that most of the precursor molecules were incorporated into a single giant network.

Figure 2b,c show qualitative mechanical testing of our elastomer. The elastomer was highly stretchable and recoverable (Figure 2b). A metal needle did not make a hole in the film (Figure 2c), demonstrating its high toughness. The video data of these experiments are available as Movie S1 (Supporting Information). The mechanical properties were quantitatively charac-

terized by uniaxial tensile testing of a ring-shaped test piece, as shown in Figure 2d. We used a tensile fixture that was able to uniformly stretch the ring because the bar supporting the ring rotated during the test. Figure 2e shows the stress–strain curves of the elastomer synthesized from the 3-arm 30k precursor. The results of three test pieces are presented to demonstrate the good reproducibility of the tests. The video data of the test is available as Movie S2 (Supporting Information). The high stretchability (stretch ratio at break $\lambda_{\text{break}} = 18.7 \pm 0.4$) and strength (stress at break $\sigma_{\text{break}} = 25.5 \pm 1.7$ MPa) are readily seen. The most unique feature is the unusual contrast in stiffness at small and large strains. The slope of the stress–strain curve abruptly increases upon stretching beyond the stretch ratio $\lambda \approx 15$.

To quantify this extraordinary strain-stiffening behavior, we calculated the tangent modulus $E_t = d\sigma_{\text{true}}/d\epsilon_{\text{true}}$ where σ_{true} is the true stress and ϵ_{true} is the true strain (Figure 2f). σ_{true} was estimated as $\sigma_{\text{true}} = \lambda\sigma_{\text{eng}}$ (σ_{eng} : engineering stress) assuming incompressibility. E_t is a measure of apparent stiffness at different stretch ratios. E_t grows from the initial value of $E_{t,\text{min}} \approx 1$ MPa to the maximum value of $E_{t,\text{max}} \approx 2000$ MPa immediately before rupture, which is a ≈ 2000 -fold difference. We also evaluated the $E_{t,\text{max}}/E_{t,\text{min}}$ of various artificial polymer materials^[2,4,15–24] and natural biological tissues^[22,25] that show strain stiffening in the literature (details are described in Section S2, Table S3, and Figures S11 and S12, Supporting Information). These reference materials include hydrogels^[19–24] and elastomers^[2,4,15–18] featuring various toughening mechanisms as well as a commercial rubber band and several biological tissues. Figure 2g shows an Ashby-type plot for $E_{t,\text{max}}/E_{t,\text{min}}$ and λ_{break} . Our elastomer is clearly in an unprecedented region that has yet to be accessed by any other soft materials known to date. Comprehensive comparison of the key properties is provided in Table S4 (Supporting Information), which highlights the excellent stretchability and toughness and unmatched strain-stiffening capability of our elastomer.

The impact of the number and length of arms in the precursor polymer was also investigated. The stress–strain curves and the tensile properties of the elastomers synthesized from 3-arm 30k, 4-arm 20k, and 4-arm 40k precursors are compared in Figure S10 and Table S2 (Supporting Information). Interestingly, the curve shape and properties, such as λ_{break} and σ_{break} , did not depend

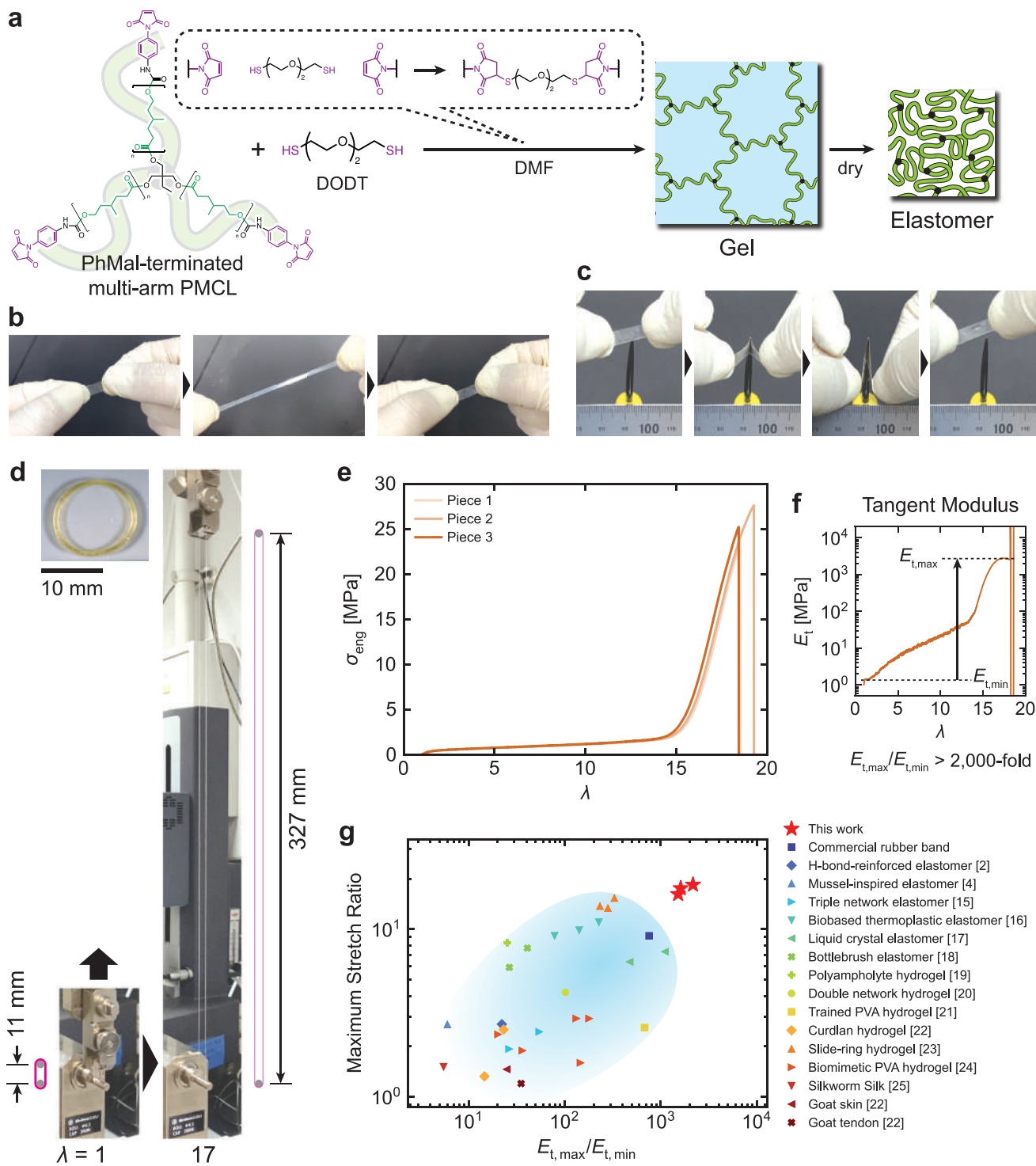


Figure 2. Preparation and mechanical properties of the module-assembled elastomer. a) Preparation scheme. PhMal-terminated multi-arm PMCL is reacted with a dithiol linker (DODT) in solution. The solvent was removed from the resultant gel, yielding a PMCL elastomer. b) Photographs showing the stretchability of the elastomer. The film was prepared from the 4-arm 20k precursor, and its dimensions were 19 mm × 7 mm × 0.25 mm. c) Photographs showing the puncture resistance of the elastomer. The sample was the same as that in (b). d) Photographs showing the ring-shaped test piece and the uniaxial tensile test. e) Stress–strain curves of the elastomer synthesized from the 3-arm 30k precursor. The stretching rate was $d\lambda/dt = 0.05 \text{ s}^{-1}$. Data for three test pieces are shown to demonstrate reproducibility. f) Tangent modulus $E_t = d\sigma_{\text{true}}/d\epsilon_{\text{true}}$ versus the stretch ratio for one of the curve (piece 3) in (e). g) Ashby-type plot of maximum stretch ratio versus strain-stiffening degree ($E_{t,\max}/E_{t,\min}$) for a wide range of stretchable polymeric materials exhibiting strain-stiffening.^[2,4,15–25] The sources of the data are described in the Supporting Information.

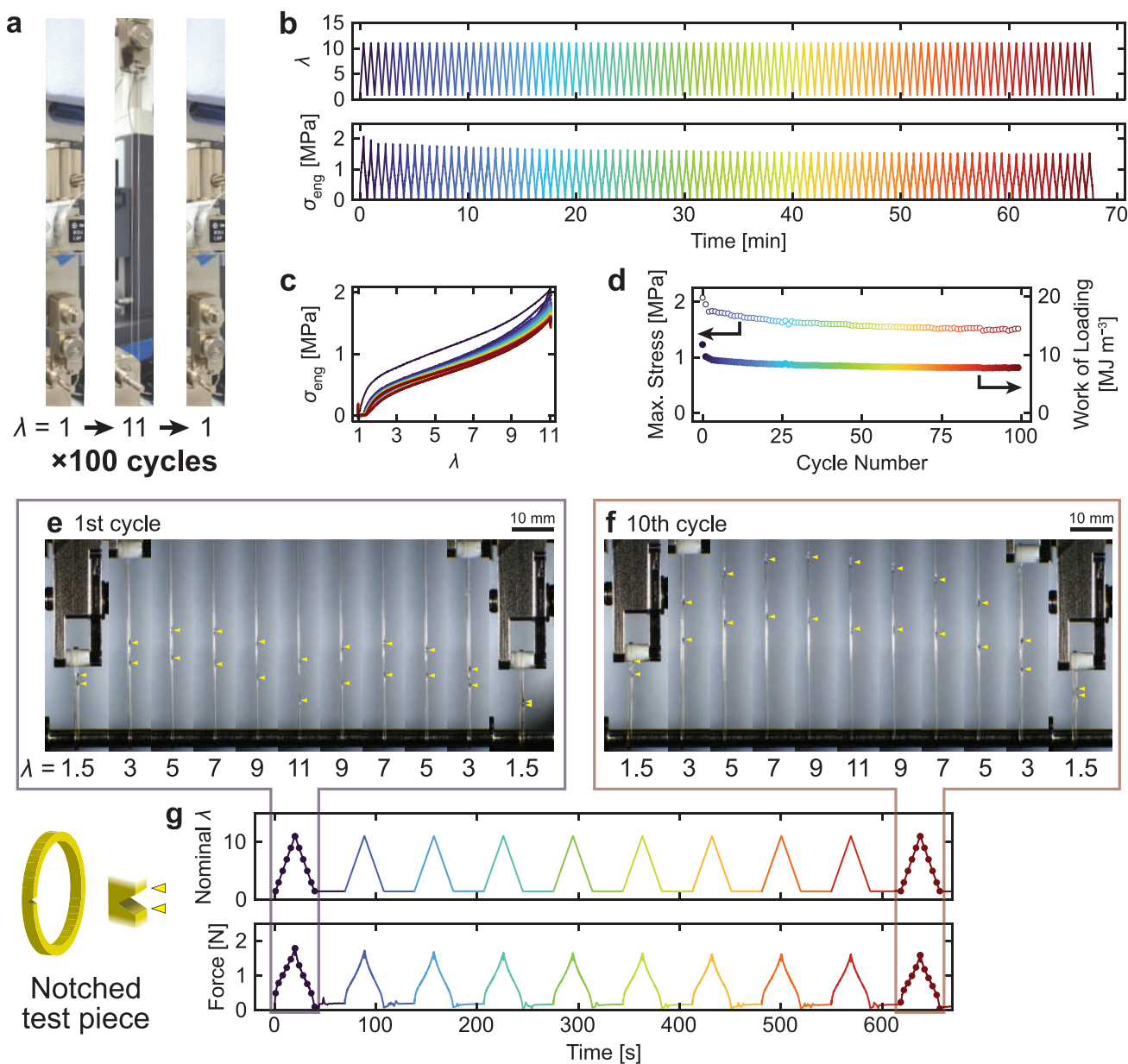


Figure 3. Mechanical durability tests of the elastomer. All elastomers were prepared from 3-arm 30k precursor. a–d) 100-cycle tensile test of a ring-shaped test piece. a) Photographs showing the deformation imposed on the test piece in a single cycle. b) Applied stretch ratio (top) and the observed engineering stress (bottom) during the 100-cycle test. c) All stress–strain curves in the 100-cycle test. The curve colors are the same as in (b). d) Maximum stress and work of loading of each cycle as a function of the cycle number. e–g) Cyclic tensile test on a notched ring test piece. A partial cut was made on a test piece and the piece was subjected to 10 loading–unloading cycles. The nominal stretch ratio was increased from 1.5 to 11 and then decreased to 1.5 in a single cycle. e,f) Photographs at different nominal stretch ratios in the first (e) and tenth (f) cycles. g) Applied nominal stretch ratio (top) and the observed tensile force (bottom) during the cyclic test. The fluctuations of the force seen between cycles are due to manual adjustment of the test piece position to keep the notch in the field of view of the microscope.

significantly on the precursor design. Even a twofold difference in arm length did not have a notable impact. These observations can be explained by the strain-stiffening mechanism of our elastomer, as we will discuss later.

The mechanical durability of our elastomer was further evaluated by two methods: cyclic loading–unloading tests and tests on a notched test piece.

Figure 3a–d shows the cyclic loading–unloading experiments on our elastomer (3-arm 30k precursor). A ring test piece was stretched from $\lambda = 1$ to $\lambda = 11$ and then released back to $\lambda = 1$ (Figure 3a). This cycle was repeated 100 times in succession without an interval. Figure 3b shows the time course of the applied λ and observed stress σ_{eng} . The stress–strain curves are shown in Figure 3c. The maximum stress and the work of loading (area

under the stress–strain curve of the loading step) initially decline but mostly remain constant over cycles (Figure 3d).

Durability against physical damage was examined using a notched ring test piece. A straight cut was made on a ring by a razor blade. The width of the cut was approximately half the width of the ring. This notched test piece was subjected to cyclic loading and unloading between the nominal stretch ratio of 1.5 and 11 over 10 cycles with a 30 s interval. Figure 3e,f shows photographs of the notched piece during the test (the video data is also available as Movie S3 (Supporting Information)). The applied nominal stretch ratio and the observed tensile force are plotted as a function of time in Figure 3g. The cut is temporarily widened upon stretching of the test piece but does not lead to catastrophic failure, indicating that crack propagation is highly suppressed. The notched piece eventually survived 10 loading–unloading cycles without rupture (Figure 3f). The excellent notch insensitivity of our elastomer is due to its large strain-stiffening capability. The region near the cut experiences larger strain than the rest of the sample and eventually becomes much stiffer due to strain stiffening. This local stiffening prevents further deformation of the region near the cut, which effectively blocks crack propagation. The notch insensitivity also contributes to the high stretchability of our elastomer. Brittle materials break at relatively low strains because even a tiny crack/defect quickly leads to a catastrophic failure. Our elastomer has the ability to stop the crack propagation by itself. This, together with the uniform stress distribution due to the homogeneous network structure, should have enabled the large λ_{break} .

3. Strain-Stiffening Mechanism

We sought to elucidate the mechanism underlying high strength and extraordinary strain-stiffening capability in our elastomer. To this end, we carried out a simultaneous uniaxial tensile test and small-angle/wide-angle X-ray scattering (tensile-SWAXS) experiment. A dumbbell-shaped test piece of the elastomer (4-arm 20k precursor) was stretched from $\lambda = 1$ to $\lambda = 13$ and then unloaded to $\lambda = 1$, during which successive SWAXS measurements were performed (Figure 4a). Representative WAXS and SAXS images are shown in Figure 4b,c, respectively, and Figure 4d,e show enlarged snapshots at each λ . The full scattering images are available as video data in Movie S4 (Supporting Information).

The WAXS image strips in Figure 4d show only a diffuse amorphous halo at low stretch ratios below $\lambda \approx 9$. However, a bright spot appears on top of this halo at $\lambda > 10$. The spot intensifies with increasing λ and diminishes upon a subsequent decrease in λ . Figure 4f shows the 1D WAXS profiles during the stretching process obtained via sector-averaging of the image in the azimuthal range of $86^\circ \leq \beta \leq 94^\circ$ (β : azimuthal angle, $\beta = 0^\circ$ and 180° correspond to the stretching direction). A major peak and a minor shoulder appear at large strains. Figure 4g is the result of the peak deconvolution analysis on the profile at $\lambda = 12.3$ assuming two pseudo-Voigt peaks on top of the amorphous halo, also modeled by a pseudo-Voigt function. The emergence of multiple scattering peaks suggests the formation of a crystal-like order by stretching. We hereafter refer to this ordering phenomenon as strain-induced ordering (SIO).

In the SAXS images in Figure 4e, a sharp streak appears along the meridian upon stretching. The 1D SAXS profiles were ob-

tained by sector-averaging over the region where the streak appeared and plotted in Figure 4h. The profiles obey a simple power law $I(q) \approx q^{-D}$ with an exponent of ≈ 3.2 , suggesting the presence of rough interfaces.^[26]

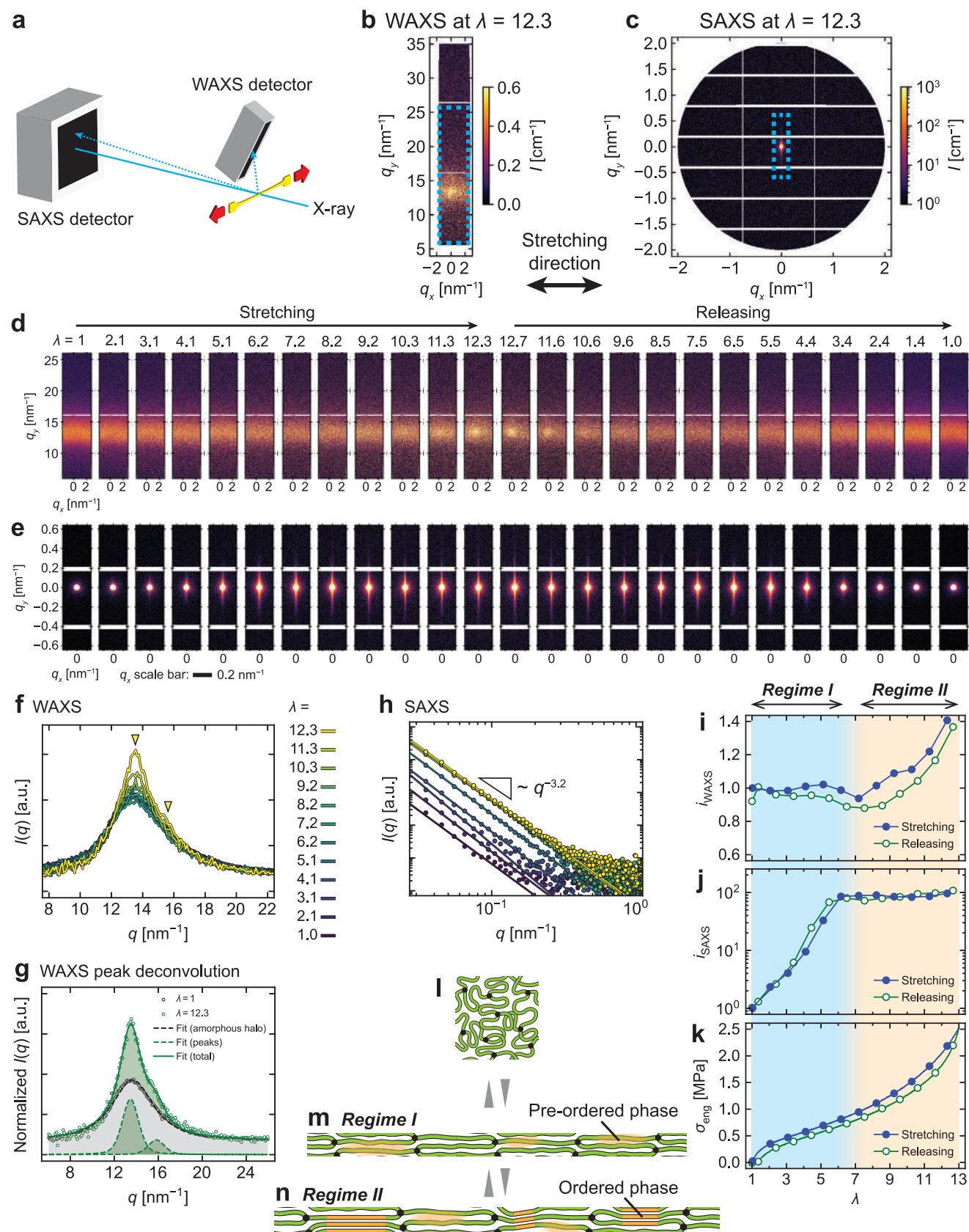
The structural evolution observed in SWAXS was quantified to gain further insight into the SIO mechanism. For WAXS, the intensity of the main peak in the 1D profiles (Figure 4f) was normalized by the initial value at $\lambda = 1$. This value is referred to as i_{WAXS} . For SAXS, the intensity at $q = 0.1 \text{ nm}^{-1}$ was normalized by the initial value at $\lambda = 1$ and referred to as i_{SAXS} . These two values and the macroscopic stress σ_{eng} are plotted against λ in Figure 4i–k. The WAXS intensity i_{WAXS} starts to increase at $\lambda \approx 7$ (Figure 4i), which roughly coincides with the onset of an upturn in the macroscopic stress σ_{eng} (Figure 4k). This observation suggests that the stiff ordered phase formed by SIO is the main cause of the extraordinary strain stiffening.

Figure 4j shows that the SAXS intensity i_{SAXS} starts to increase with λ from the very beginning of stretching, which is different from the behavior of i_{WAXS} . Even more interestingly, i_{SAXS} stops increasing at $\lambda \approx 6$. We hypothesize that the SAXS intensity arises from a preordered phase formed prior to the SIO seen in WAXS. In the region below $\lambda \approx 6$ (assigned as regime I in Figure 4i–k), a preordered phase with rough interfaces gradually grows due to moderate elongation of the network strands (Figure 4m). Then, the preordered phase turns into a more ordered phase at strains beyond $\lambda \approx 7$ (regime II, Figure 4n), resulting in the emergence of the distinct WAXS peaks.

Another interesting observation here is the small but finite hysteresis in both i_{WAXS} and σ_{eng} , i.e., lower values in the releasing process than in the stretching process. We speculate that the SIO is path-dependent, i.e., the ordered phase is slightly less stable in the releasing process (= negative strain rate) compared to that in the stretching process (= positive strain rate). This would have led to a lower macroscopic stress in the releasing process and thus to the mechanical hysteresis, which we could also confirm in Figure 3c. Further investigation on the SIO including the strain rate dependence is needed to fully understand this phenomenon.

Earlier, we found that the strain-stiffening behavior did not depend significantly on the precursor architecture (arm number and molecular weight, Figure S10, Supporting Information). In particular, both the onset λ of strain stiffening and the λ at break were similar between the elastomer synthesized from 4-arm 20k precursor and that from 4-arm 40k precursor, despite the ≈ 2 -fold difference in the average chain length between crosslinks. If the strain stiffening were caused by chains approaching to a fully extended conformation, its onset λ would have depended significantly on the chain length. A possible explanation is that the SIO behavior is mainly governed by the strain field within the material, rather than how close the chains are to their fully extended state. The densely packed PMCL chains in our elastomers would experience a similar homogeneous strain field at a given λ due to structural homogeneity, leading to similar strain-stiffening behavior regardless of the chain length between crosslinks.

There are some examples of strain-induced crystallization (SIC) in crosslinked polymers. Natural rubber, which mainly consists of all-*cis* 1,4-polyisoprene, undergoes SIC.^[27] Recently, SIC has been observed in poly(ethylene glycol) (PEG) hydrogels subjected to large strains.^[23,28] These polymers that show SIC



(e.g., natural rubber and PEG) are crystallizable in the quiescent melt state. In the present work, however, PMCL is totally non-crystallizable in its quiescent state because of the isomeric irregularity of the methyl side group. Here, we have shown that even a non-crystallizable stereo-irregular polymer can form an ordered phase when subjected to extreme strain in a highly homogeneous network.

4. Application for a Mechanically Simple Variable Stiffness Actuator

Our elastomer offers potential in various applications that require high mechanical strength, stretchability, and nonlinear response, including fields such as robotics, flexible electronics, replacement for biological tissues, etc. Here, we demonstrate the application of our elastomer as a component in a variable stiffness actuator (VSA).^[29–31] Unlike conventional rigid actuators, VSAs offer great flexibility that is crucial for use in human-friendly, safe, and dexterous robots. However, VSAs generally require complicated and bulky mechanisms when ordinary linear springs are used as the elastic component. The use of tough and highly nonlinear elastic components can greatly simplify VSA designs. To test this hypothesis, we built a simple antagonistic joint-type VSA consisting of a linear stage and a rotatable joint coupled through a pair of elastomer tendons (Figure 5a). The tension of the elastomer tendons is adjusted through gap d , and the tension regulates the stiffness of the joint. The apparent stiffness of the joint was evaluated by measuring the force f_n needed to push down the apparatus by distance z against the rigid floor (Figure 5b,c and Movie S5, Supporting Information). Figure 5d shows the f_n - z curve obtained with various d values. The pushing force increases significantly with increasing d . We defined the initial slope of the f_n - z curve as the apparent stiffness k_a . Figure 5e shows k_a evaluated for various d values. The 16-fold variation in the stiffness is achieved simply by loosening or stretching the elastomer tendons. Moreover, the observed stiffness agrees well with a numerical simulation based on the tensile property of the elastomer (solid curve in Figure 5e; details of the simulation can be found in Section S5, Supporting Information). This data sharply contrasts the case where linear springs were used as the tendons: the simulation showed a stiffness variability of up to 3-fold with typical commercially available linear tension springs (Figure S19, Supporting Information). We further demonstrated the excellent stiffness variability of our VSA by investigating the interaction with a soft and fragile object, a block of Japanese silken tofu (Figure 5f). The video data of this experiment is avail-

able as Movie S6 (Supporting Information). When the elastomer tendons are loosened (Figure 5g), the finger is highly compliant and thus can touch the tofu block softly without damage (Figure 5h). Once the elastomer is highly stretched (Figure 5i), the finger is stiff and can break the tofu block (Figure 5j,k). The wide variation of touching force is also shown in Figure 5l where f_n is plotted against z . The wide stiffness variability demonstrated here is realized only by stretching and loosening of the elastomer without complicated and bulky mechanisms. The unprecedented strain-stiffening nature, together with the excellent mechanical reliability, will lead to new possibilities not only in robotics but also in flexible electronics, biomedical applications, etc.

5. Conclusion

We developed a tough elastomer with extraordinary strain-stiffening capability by realizing a highly homogeneous network structure via the module-assembly strategy. The elastomers were synthesized by end-linking monodisperse star polymers with low T_g . In addition to high stretchability and strength, the elastomers showed significant strain stiffening upon stretching beyond a certain critical stretch ratio. This combination of high stretchability and strain-stiffening capability exhibited by our elastomer exceeded the performance of any other soft materials known to date. Its high resilience against repeated mechanical loading and its notch-insensitive nature were also demonstrated. Tensile-SWAXS analysis suggested strain-induced ordering of polymer chains, which was determined to be the cause of the large strain stiffening. We finally demonstrated the use of our elastomer as a component in a variable stiffness actuator in which the highly nonlinear mechanical response of the elastomer played a central role. We propose that the unique mechanical function of the developed elastomer can open up new possibilities in a wide range of engineering fields, such as soft robotics, flexible electronics, and biomedical applications.

6. Experimental Section

Materials: 3,6-Dioxa-1,8-octanedithiol (DODT), diphenyl phosphate (DPP), di(trimethylolpropane) (DTMP), and trimethylolpropane (TMP) were purchased from Tokyo Chemical Industry Co. Ltd (Japan). Dibutyltin dilaurate (DBTDL), dry toluene, dry dichloromethane (DCM), and dry ethanol were purchased from FUJIFILM Wako Pure Chemical Corp. (Japan). All reagents were used as received unless otherwise noted. 4-Methyl- ϵ -caprolactone (mixture of isomers) (MCL)^[32] and

Figure 4. Tensile-SWAXS analysis of the elastomer synthesized from the 4-arm 20k precursor. a) Layout of the experiment. The test piece was stretched from $\lambda = 1$ to 13 at the rate of $d\lambda/dt = 0.1 \text{ s}^{-1}$ and immediately unloaded at the same rate. SWAXS measurements were performed successively during this process. b) WAXS and c) SAXS images collected at $\lambda = 12.3$. Blue dashed rectangles indicate the display range in (d) and (e). d) WAXS and e) SAXS images at each λ during stretching and releasing. The areas indicated by dotted rectangles in (d) and (e) are shown. f) 1D WAXS profiles obtained by sector-averaging over the azimuthal angle range of $86^\circ \leq \beta \leq 94^\circ$. A peak and a shoulder appearing at large strains are indicated by triangles. g) Results of the peak deconvolution analysis for the 1D WAXS profile at $\lambda = 1$ and 12.3. The intensities were normalized by the integrated intensity in the q range of $21\text{--}26 \text{ nm}^{-1}$. First, the amorphous halo at $\lambda = 1$ was fitted with a pseudo-Voigt function. This intensity of the amorphous halo was used as the baseline for fitting at $\lambda = 12.3$, where two more pseudo-Voigt functions were added to model the additional peak and shoulder. The widths of these two functions were constrained to be equal during curve fitting. h) 1D SAXS profiles obtained by sector-averaging over the limited region on the 2D image where the streak appears. The solid lines represent the linear fitting results according to the power-law model $I(q) = Aq^{-D}$. Symbol/line colors are the same as in (g). i) Normalized WAXS peak intensity (I_{WAXS}), j) normalized SAXS intensity at $q = 0.1 \text{ nm}^{-1}$ (I_{SAXS}), and k) macroscopic engineering stress σ_{eng} of the elastomer during stretching and releasing. l–n) Schematic illustration of the proposed SIO mechanism. l) Before stretching. m) Regime I. Preordered phases with rough interfaces are formed. n) Regime II. Crystal-like ordered phases are formed.

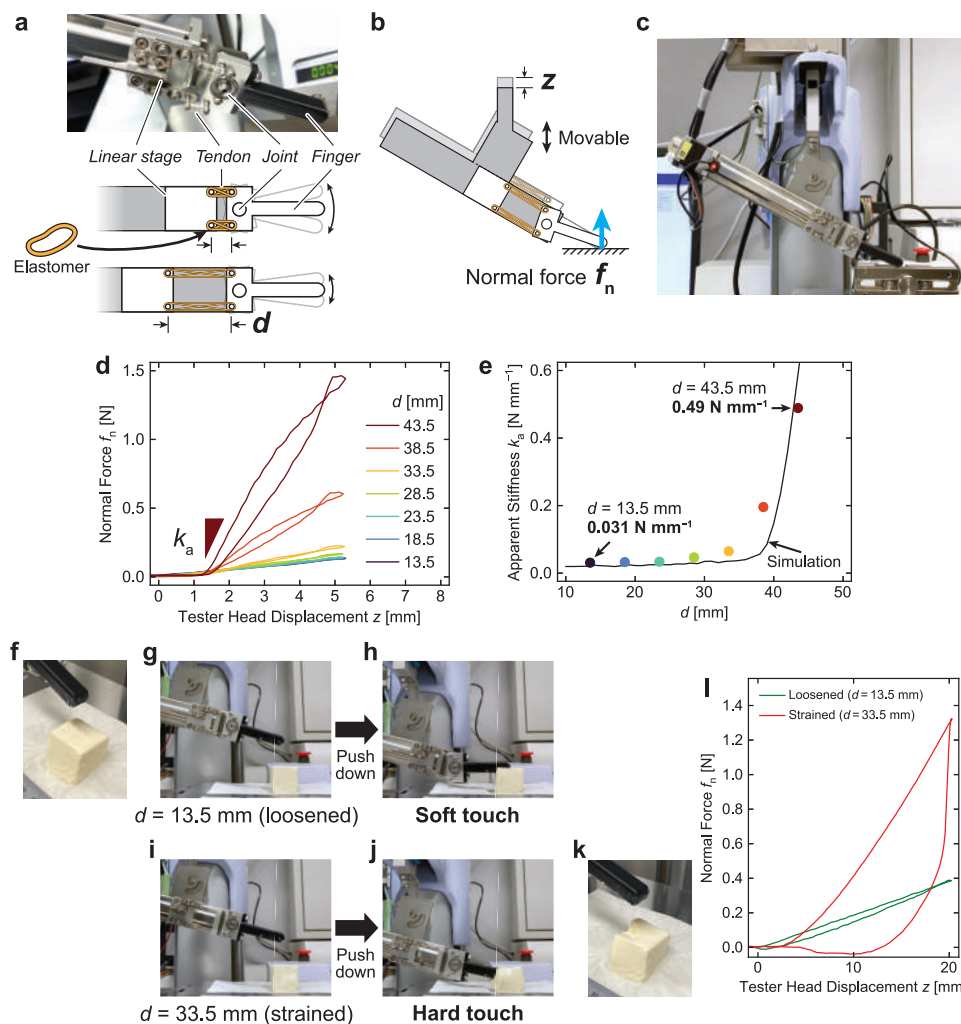


Figure 5. Design and evaluation of a model VSA. a) Photograph and schematic illustration of the core components of the VSA. b,c) Schematic illustration and corresponding photograph of the experimental setup to measure the stiffness of the VSA. d) Normal force f_n plotted against tester head displacement z during pushing and releasing cycles with different values of gap distance d . e) Observed apparent stiffness at each d value (filled circles). The simulation result is shown as a solid curve. f–l) Demonstration experiment of the VSA using a soft and fragile tofu block. f) Pristine tofu block prior to the experiment. The size was $\approx 25 \text{ mm} \times 25 \text{ mm} \times 25 \text{ mm}$. g,h) Pushing down the VSA toward the tofu block with elastomer tendons loosened ($d = 13.5 \text{ mm}$). i,j) Pushing down the VSA with tendons strained ($d = 33.5 \text{ mm}$). k) Damaged tofu block after the experiment. l) Normal force plotted against the vertical displacement of the tester.

p-maleimidophenyl isocyanate (PMPI)^[12] were synthesized according to the literature.

Characterization: ^1H NMR spectra were recorded on an ECZ-600R spectrometer (JEOL, Japan). Size exclusion chromatography (SEC) measurements were performed using a Nexera SEC system (Shimadzu, Japan) with a triple detector (OmniSEC Reveal, Malvern Panalytical, UK). The column and the eluent were a TSKgel GMHHR-M (Tosoh, Japan) and chloroform, respectively. The measurements were conducted at 40°C .

Synthesis of OH-Terminated Multi-Arm PMCL: The synthesis of OH-terminated 4-arm 40k is described as an example. A 200 mL Erlenmeyer flask with a stirrer bar and a 50 mL screw vial were dried in a 100°C oven. DPP (4.999 g; 19.98 mmol) was weighed in the dried 50 mL vial. DTMP (125.4 mg; 0.5009 mmol) was weighed in a 5 mL plastic tube. The flask, the vial, and the plastic tube were brought into a nitrogen-filled glove box. In the glove box, the Erlenmeyer flask was charged with MCL (24.89 mL; $\approx 25.6 \text{ g}$ assuming the same density as ϵ -caprolactone, 1.03 g mL^{-1} ; $\approx 200 \text{ mmol}$) and DTMP. DPP in the vial was dissolved in dry toluene (25 mL) and the solution was added to the Erlenmeyer flask to initiate the

polymerization. The progress of the reaction was monitored by SEC. The reaction was stopped by neutralizing DPP with excess triethylamine after 200 min. The crude mixture was poured into methanol, and the viscous precipitate was separated by centrifugation. This was repeated 4 times in total. A small amount of low-molecular-weight fraction was observed in SEC, presumably due to initiation from water. Therefore, the desired high-molecular-weight fraction was isolated by repeated fractional precipitation using tetrahydrofuran as a good solvent and methanol as a poor solvent. The product was finally collected in a glass vial and dried in vacuum at r.t. to obtain a colorless viscous liquid, 11.7 g (46% based on the monomer feed). The ^1H NMR spectrum is shown in Figure S3 (Supporting Information). See Table S1 (Supporting Information) for characterization results. The other OH-terminated multiarm PMCLs were synthesized in a similar manner. The initiator feed was varied to obtain the desired molecular weight. For 3-arm PMCL, TMP was used as the initiator.

Synthesis of PhMal-Terminated Mutli-Arm PMCL: Here, the synthesis of PhMal-terminated 4-arm 40k is presented as an example. Hydroxy-terminated 4-arm PMCL ($M_n = 40 \text{ kDa}$; 2.00 g; 0.05 mmol; 0.20 mmol

hydroxy end groups), PMPI (267.8 mg; 1.39 mmol; 7.0 eq. against hydroxy), and DBTDL (78.7 mg; 0.125 mmol; $\approx 9\%$ against isocyanate) were separately taken in oven-dried screw vials and brought into a nitrogen-filled glove box with an oven-dried 500 mL Erlenmeyer flask. In the glove box, the polymer was dissolved in dry DCM (20 mL) in the vial. PMPI and DBTDL were dissolved in dry DCM (60 mL) in the Erlenmeyer flask. The polymer solution was added dropwise to the flask, with an additional 20 mL of dry DCM to collect the remaining polymer in the vial. The pale yellow solution was stirred overnight in the glove box. Then, dry ethanol (1 mL) was added to the flask to quench the excess isocyanate. After stirring the mixture for several hours, the flask was removed from the glove box. The mixture was concentrated on a rotavapor and precipitated in methanol 4 times. At this stage, the product contained insoluble solids, which may be residual urea. To remove the insoluble part, the product was dissolved in a minimal amount of toluene, and the solution was filtered through a syringe filter. Drying out toluene by nitrogen stream and then in vacuum at r.t. gave the product as a yellow viscous liquid, 2.06 g ($\approx 100\%$). The ^1H NMR spectrum is shown in Figure S7 (Supporting Information). See Table S1 (Supporting Information) for characterization results. The synthesis of PhMal-terminated PMCLs with different arm numbers and molecular weights was conducted in a similar manner.

Fabrication of Module-Assembled Elastomers: In a typical experiment, the polymer (40 mg) was taken in a small glass tube. In a nitrogen-filled glove box, dry DMF (180 μL) was added to the tube and the polymer was dissolved. A DMF solution of DODT with a prescribed concentration (20 μL) was added, and the tube was vigorously shaken for several tens of seconds to homogenize the solution. The solution was carefully injected into a mold with a micropipette, sealed, and cured for 2 days at r.t. in the glove box. The gel was then removed from the mold and dipped in dry DMF for 1 day, in a 1:1 mixture of DMF and toluene for another 1 day, and then in toluene for more than 3 days. The gel fully swollen with toluene was finally dried in air and in vacuum at r.t. for over a week, yielding a pale brown transparent elastomer. Two types of molds were used to produce ring-shaped test pieces with rectangular cross sections and dumbbell-shaped test pieces. The ring test pieces typically had the thickness of 0.55 mm, width of 1.1 mm, and inner diameter of 11 mm. The shape of the dumbbell test pieces was 1/4-scale of ISO 37-1A (JIS K6251-3) with a thickness of ≈ 0.1 mm.

Uniaxial Tensile Test: Uniaxial tensile tests were conducted using a universal tester (EZ-L, Shimadzu, Japan) equipped with a fixture for ring-shaped test pieces. The fixture consisted of two bars, one of which rotated during the test to ensure uniform stretching of the ring test piece. The stretch ratio was calculated as $\lambda = 2x/L_{\text{inner}}$, where x is the crosshead displacement and L_{inner} is the initial inner circumference of the ring test piece. The engineering stress was calculated as $\sigma_{\text{eng}} = F/(2S)$ where F is the tensile force and S is the cross-sectional area of the ring. For cyclic tensile tests on a notched test piece (Figure 3e–g), the test piece position was manually adjusted by tweezers during the 30 s interval between cycles, so that the crack part was kept in the field of view of the microscope used to capture the images during the tests.

Simultaneous Tensile Test and Small-Angle/Wide-Angle X-ray Scattering Measurements (Tensile-SWAXS): The tensile-SWAXS experiment was performed on a small-angle instrument installed at beamline BL-15A2 in Photon Factory, High Energy Accelerator Research Organization, Tsukuba, Japan.^[33] A custom-made tensile tester was mounted on the sample stage. Details of the tensile tester are described elsewhere.^[34] A dumbbell-shaped test piece was fixed to the clamps. The position of the test piece relative to the incident X-ray beam was carefully adjusted so that the beam hit the center of the straight section of the test piece. The test piece was uniaxially stretched at the rate of $d\lambda/dt = 0.1 \text{ s}^{-1}$ from $\lambda = 1$ to $\lambda = 13$ and immediately unloaded to $\lambda = 1$ at the same rate. The force was recorded by a load cell connected to one of the clamps. SWAXS measurements were performed periodically during the test. The exposure time for each frame was 1 s, and the interval between the start times of consecutive frames was ≈ 10 s. The wavelength of the incident X-ray beam Λ was 0.1200 nm. The incident and transmitted X-ray intensities were monitored by an ionization chamber in front of the sample and a photodiode at the direct beam stopper, respectively. The scattered X-ray was collected by two 2D detectors

(for WAXS: PILATUS3 300K-W, for SAXS: PILATUS3 2 M, Dectris, Switzerland). The sample-to-detector distances for the WAXS and SAXS detectors were 425 mm and 3210 mm, respectively. The WAXS detector was tilted toward the sample by 23° . The direct beam position and the sample-to-detector distance were calibrated by using silver behenate (for SAXS and WAXS) and cerium oxide (for WAXS) standards. The collected data were analyzed by using custom-made Python scripts. The scattering images were corrected for incident beam flux, exposure time, absorption, solid angle coverage of the detector pixels, and background scattering.

Evaluation of the Variable Stiffness Actuator (VSA): The custom-made apparatus for the VSA experiments consisted of a motorized linear stage, a ball-bearing joint, and a 3D-printed finger (see Figure 5a). Two elastomer bands made from the 3-arm 30k precursor were used. The cross section of the band was $\approx 1 \text{ mm} \times 0.6 \text{ mm}$, and the inner diameter in the loosened state was $\approx 3.9 \text{ mm}$. Each band was wrapped twice around the two pins on the stage and the joint. The linear stage was fixed to a universal tester (EZ-L, Shimadzu, Japan) through a steel fixture (Figure 5c). To evaluate the apparent stiffness of the joint, the tester head position z was changed from -10.0 to 5.3 mm and then back to -10.0 mm at a speed of 150 mm min^{-1} , during which the vertical force was recorded by the tester. The origin of z was set to the point where the tip of the finger component just touched a rigid steel block. Then, the linear stage gap d was incremented by 5 mm to vary the tension on the elastomer tendons. These processes were repeated for d values of 13.5, 18.5, 23.5, 28.5, 33.5, 38.5, and 43.5 mm. The detailed setup is described in the Supporting Information (Section S4, Supporting Information).

Supporting Information

Supporting Information is available from the Wiley Online Library or from the author.

Acknowledgements

S.N. acknowledges JACI Prize for Encouraging Young Researcher. This work was supported by JSPS KAKENHI Grant No. 21K14678. The SWAXS experiments were performed under the approval of the Photon Factory Advisory Committee (proposal No. 2021G096).

Conflict of Interest

The authors declare no conflict of interest.

Data Availability Statement

The data that support the findings of this study are available from the corresponding author upon reasonable request.

Keywords

crosslinking, elastomers, robotics, strain stiffening

Received: February 5, 2023

Revised: March 7, 2023

Published online:

- [1] G. Heinrich, M. Klüppel, T. A. Vilgis, *Curr. Opin. Solid State Mater. Sci.* **2002**, 6, 195.

- [2] J. Wu, L.-H. Cai, D. A. Weitz, *Adv. Mater.* **2017**, *29*, 1702616.
- [3] S. Yoshida, H. Ejima, N. Yoshie, *Adv. Funct. Mater.* **2017**, *27*, 1701670.
- [4] E. Filippidi, T. R. Cristiani, C. D. Eisenbach, J. H. Waite, J. N. Israelachvili, B. K. Ahn, M. T. Valentine, *Science* **2017**, *358*, 502.
- [5] Y. Miwa, J. Kurachi, Y. Kohbara, S. Kutsumizu, *Commun. Chem.* **2018**, *1*, 5.
- [6] T. Sakai, T. Matsunaga, Y. Yamamoto, C. Ito, R. Yoshida, S. Suzuki, N. Sasaki, M. Shibayama, U. Chung, *Macromolecules* **2008**, *41*, 5379.
- [7] X. Li, S. Nakagawa, Y. Tsuji, N. Watanabe, M. Shibayama, *Sci. Adv.* **2019**, *5*, eaax8647.
- [8] S. Nakagawa, N. Yoshie, *Polym. Chem.* **2022**, *13*, 2074.
- [9] M. Ohira, T. Katashima, M. Naito, D. Aoki, Y. Yoshikawa, H. Iwase, S. Takata, K. Miyata, U. Chung, T. Sakai, M. Shibayama, X. Li, *Adv. Mater.* **2022**, *34*, 2108818.
- [10] G. X. De Hoe, M. T. Zumstein, B. J. Tiegs, J. P. Brutman, K. McNeill, M. Sander, G. W. Coates, M. A. Hillmyer, *J. Am. Chem. Soc.* **2018**, *140*, 963.
- [11] D. C. Batiste, M. S. Meyersohn, A. Watts, M. A. Hillmyer, *Macromolecules* **2020**, *53*, 1795.
- [12] R. Takashima, J. Kida, D. Aoki, H. Otsuka, *J. Polym. Sci., Part A: Polym. Chem.* **2019**, *57*, 2396.
- [13] R. Takashima, M. Ohira, H. Yokochi, D. Aoki, X. Li, H. Otsuka, *Soft Matter* **2020**, *16*, 10869.
- [14] J. M. J. M. Ravasco, H. Faustino, A. Trindade, P. M. P. Gois, *Chemistry* **2019**, *25*, 43.
- [15] E. Ducrot, Y. Chen, M. Bulters, R. P. Sijbesma, C. Creton, *Science* **2014**, *344*, 186.
- [16] A. Watts, N. Kurokawa, M. A. Hillmyer, *Biomacromolecules* **2017**, *18*, 1845.
- [17] H. Kim, J. M. Boothby, S. Ramachandran, C. D. Lee, T. H. Ware, *Macromolecules* **2017**, *50*, 4267.
- [18] M. Vatankhah-Varnosfaderani, W. F. M. Daniel, M. H. Everhart, A. A. Pandya, H. Liang, K. Matyjaszewski, A. V. Dobrynin, S. S. Sheiko, *Nature* **2017**, *549*, 497.
- [19] T. L. Sun, T. Kurokawa, S. Kuroda, A. B. Ihsan, T. Akasaki, K. Sato, M. A. Haque, T. Nakajima, J. P. Gong, *Nat. Mater.* **2013**, *12*, 932.
- [20] T. Nakajima, Y. Ozaki, R. Namba, K. Ota, Y. Maida, T. Matsuda, T. Kurokawa, J. P. Gong, *ACS Macro Lett.* **2019**, *8*, 1407.
- [21] S. Lin, J. Liu, X. Liu, X. Zhao, *Proc. Natl. Acad. Sci. USA* **2019**, *116*, 10244.
- [22] C. Wu, J. Huang, B. Chu, J. Deng, Z. Zhang, S. Tang, X. Wang, Z. Wang, Y. Wang, *ACS Nano* **2019**, *13*, 10727.
- [23] C. Liu, N. Morimoto, L. Jiang, S. Kawahara, T. Noritomi, H. Yokoyama, K. Mayumi, K. Ito, *Science* **2021**, *372*, 1078.
- [24] J. Luo, S. Li, J. Xu, M. Chai, L. Gao, C. Yang, X. Shi, *Adv. Funct. Mater.* **2021**, *31*, 2104139.
- [25] C. Guo, J. Zhang, X. Wang, A. T. Nguyen, X. Y. Liu, D. L. Kaplan, *Small* **2017**, *13*, 1702266.
- [26] J. S. Higgins, H. C. Benoit, *Polymers and Neutron Scattering*, Oxford University Press, Oxford, UK, **1994**.
- [27] M. Tosaka, *Polym. J.* **2007**, *39*, 1207.
- [28] T. Fujiyabu, N. Sakumichi, T. Katashima, C. Liu, K. Mayumi, U. Chung, T. Sakai, *Sci. Adv.* **2022**, *8*, eabk0010.
- [29] G. Tonietti, R. Schiavi, A. Bicchì, in *Proc. 2005 IEEE Int. Conf. on Robotics and Automation*, IEEE, Piscataway, NJ, USA **2005**, pp. 526–531.
- [30] N. G. Tsagarakis, I. Sardellitti, D. G. Caldwell, in *2011 IEEE/RSJ Int. Conf. on Intelligent Robots and Systems*, IEEE, Piscataway, NJ, USA **2011**, pp. 378–383.
- [31] V. Grosu, C. Rodriguez-Guerrero, S. Grosu, B. Vanderborght, D. Lefeber, *IEEE ASME Trans. Mechatron.* **2017**, *22*, 1777.
- [32] J. L. Self, C. S. Sample, A. E. Levi, K. Li, R. Xie, J. R. de Alaniz, C. M. Bates, *J. Am. Chem. Soc.* **2020**, *142*, 7567.
- [33] H. Takagi, N. Igarashi, Y. Nagatani, H. Ohta, T. Mori, T. Kosuge, N. Shimizu, *AIP Conf. Proc.* **2019**, *2054*, 060038.
- [34] S. Nakagawa, N. Yoshie, *Soft Matter* **2022**, *18*, 4527.